applied sciences

MDPI

Article

The Mesoscopic Numerical Simulation of GAP/CL20/AP Composite Solid Propellant Based on MPM and FEM

Xiaoyong Gu [1], Xiangyang Liu [2,*], Chunying Dong [2], Guanglong Zhang [2], Liming Zhang [1] and Fengjian Zhang [1]

[1] School of Civil and Transportation Engineering, Henan University of Urban Construction, Pingdingshang 467036, China
[2] School of Aerospace Engineering, Beijing Institute of Technology, Beijing 100081, China; cydong@bit.edu.cn (C.D.)
* Correspondence: liuxy@bit.edu.cn; Tel.: +86-010-68912406

Featured Application: Based on experiments and mesoscopic numerical simulation methods, this paper analyzes the correlation between the meso-structural state and macro-mechanical properties, which is of great significance in the prediction of macro-mechanical properties of composite propellants, the analysis of meso-failure mechanisms, and the structural design of propellants.

Abstract: In this paper, first, the meso-debonding process of a GAP/CL20/AP composite solid propellant under uniaxial tension was analyzed using the advantages of the material point method (MPM) and the finite element method (FEM) for the first time; then, the numerical simulation results were compared with the experiments. Based on the basic principle of modeling with the material point method, grains of different sizes were generated quickly and efficiently. Next, the grains were dispersed into particles, and the position information of the particles was mapped onto the background grid, so the background grids were used to determine the position of the grains. After that, the generated AP and CL20 grains were imported into the commercial software Abaqus through python scripting codes for numerical calculation. Based on macro-mechanical tests and a micro-numerical simulation, this paper studies the micro-internal mechanism that affects the macro-mechanical properties of composite solid propellants. Three interface parameters needed to be determined by parameter inversion, and the value of the objective interpolation function min$R$ was 0.05078%. From a comparison, it was found that the numerical simulation results are in good agreement with the experimental results in the aspects of micro-crack cracking characteristics and the nominal stress–strain curve of propellants. After that, the influence of interface parameters on the stress–strain curve are discussed. The research in this paper has high scientific value and engineering application value and can provide important reference and guidance for the design of composite solid propellants and its mechanical property analyses, so as to solve the structural integrity problem of solid rocket motor charges.

Keywords: MPM; FEM; mechanical properties; micro-model of propellants

check for updates

Citation: Gu, X.; Liu, X.; Dong, C.; Zhang, G.; Zhang, L.; Zhang, F. The Mesoscopic Numerical Simulation of GAP/CL20/AP Composite Solid Propellant Based on MPM and FEM. *Appl. Sci.* **2023**, *13*, 4552. https://doi.org/10.3390/app13074552

Academic Editor: Francesco Tornabene

Received: 21 February 2023
Revised: 26 March 2023
Accepted: 27 March 2023
Published: 3 April 2023

Copyright: © 2023 by the authors. Licensee MDPI, Basel, Switzerland. This article is an open access article distributed under the terms and conditions of the Creative Commons Attribution (CC BY) license (https://creativecommons.org/licenses/by/4.0/).

1. Introduction

With the rapid development of modern weapons, the comprehensive performance requirements of new solid propellants are getting higher and higher [1]. In order for the propellant to meet the demanding requirements of high energy and high performance, the most effective way is to use an energetic binder (such as a glycidyl azide polymer (GAP)) instead of a non-energetic binder. With high heat generation and high density, GAP is an excellent energetic adhesive. However, for a long time, research on the mechanical properties of gap-based composite solid propellants was limited to their macro-mechanical properties. For example, the macroscopic mechanical properties of propellants are studied via uniaxial tensile dumbbell-shaped specimens. However, this method can only provide

the mechanical properties of a propellant in the static and macroscopic states. In the process of stretching, it is difficult to characterize the microstructure evolution of the propellant. Therefore, this method cannot meet the development needs of new weapon platforms.

Meso-debonding is a common failure mechanism in composite solid propellants, initiated by the build-up of stress within the propellant due to thermal and mechanical loads. This stress can cause micro-cracks to form at the interface between the solid particles and the binder. Over time, these micro-cracks can grow and coalesce, leading to the formation of meso-cracks. Once meso-cracks form, the binder and the solid particles are no longer fully bonded, and the propellant may start to show signs of degradation. This can lead to reduced mechanical properties and a decrease in the overall performance of the rocket engine. The macro-mechanical behavior of composite solid propellants strongly depends on the microstructure, so under an external load, micro-cracks, the expansion of micro-holes, and local high stress and strain may destroy the microstructure of interface bonding, leading to interfacial debonding between the grains and the matrix and then affecting the macro-mechanical properties [2]. In recent years, scholars have carried out a lot of work in order to study the meso-mechanical characteristics and damage evolution processes of propellants in depth. Liu et al. found that the interface between particles and matrix was the starting point of hydroxyl-terminated polybutadiene (HTPB) propellant failure [3,4]. In order to describe the mechanical properties of propellant more accurately, Cui et al. [5] learned through experiments that the mechanical properties of a propellant are related to its loading rate. Through uniaxial tensile tests at different temperatures and strain rates, Zhang et al. [6] found that a numerical simulation only considering interfacial debonding between the propellant particles and the matrix could not accurately predict the failure behavior of a propellant, so it was inferred that the failure of a propellant also included the damage to the matrix. Via scanning electron microscopy, Zhou [7] found that the failure of a propellant included debonding between the particles and the matrix, and the wire drawing failure of the matrix.

However, due to the limitations of experimental methods, it is impossible to quantitatively analyze the meso-damage evolution process of high-energy materials, so the numerical simulation method has become an effective method of analyzing the interface failure of multiphase materials in recent years. By using a single particle axisymmetric mesoscopic model, Chen et al. [8] studied the stress concentration factor and adhesion failure angle of a nitrate plasticized polyether (NEPE) propellant under different solid contents and bonding agents. Matous et al. [9] used the molecular dynamics method to generate the representative volume element of a propellant and studied the damage and failure of a particle interface under the conditions of a small strain, which proved that the interface damage was the main reason for the nonlinear mechanical properties. Based on Matou's research, Inglis [10] used elliptic particles to carry out numerical calculations, and it is known that the damage evolution process of the model is divided into three stages: the elastic stage, the stage where interfacial debonding occurs between the particles and the matrix, and large deformation of the matrix stage.

By establishing the random particle-filled mesoscopic numerical model, Rae et al. [11] described the macro-meso damage evolution process of a propellant interface and a matrix as independent phases, in which the interface is often regarded as the main damage mode of the microstructure of particle-filled polymer materials. By establishing a two-dimensional random filling model of circular particles, Chang and others [12–16] simulated the process of uniaxial tension and stress relaxation of a propellant and described the interfacial debonding with a cohesion element. Francqueville, etc. [17,18] thought that particles in the propellant had spherical and polyhedral geometries, so the three-dimensional model filled with spherical and polyhedral particles was used to simulate the damage evolution of a propellant during a quasi-static stretching process. Ruize [19] and Prakash [20,21] embedded a single ammonium perchlorate (AP) in HTPB, and its interface parameters were determined with a Raman spectrometer and an impact test, and the interfacial debonding was studied using a linear cohesive unit model. MATOUS [22] and others [23,24] considered

the influence of particles with different sizes and interface parameters, but there were some differences between the numerical model and the real structure of the propellant.

However, many scholars have carried out numerical simulations on the micromechanical properties and microstructure evolution of NEPE and HTBP propellants. In 2006, Yuan Song and others [25] established a micro-finite element model of composite solid propellants via a numerical simulation. Based on the stress distribution between the particles and matrix, the failure mechanism of the propellant was studied at the meso level. They found that large grains were easier to debond under an external load, and grain debonding was the main reason for the failure of a solid propellant. In 2007, Inglis and Geubelle et al. [26] established a mesoscopic model of composite propellants. The debonding between particles and binder matrix was realized by traction–separation laws, and the damage evolution process of the composite materials was analyzed by the multi-scale finite element method. They found that large particles were more prone to dewetting, and small particles could only increase the initial modulus of the matrix, so it was not necessary to model small particles. In 2017, Han et al. [27] established a mesoscopic calculation model of propellants with cohesive constitutive elements; they found that the randomness of the particles did not affect the macroscopic mechanical behavior of propellant. In 2021, Franqueville [17] etc. established three-dimensional meso-numerical models of three propellants using the mesostructure generation algorithm, and the debonding at the matrix/filler interface was considered in the process of model establishment. They compared the stress–strain relation obtained by numerical simulation with the experiment and discussed the influence of cohesive parameters on the macro stress–strain relation. However, the amount of research on the micromechanical properties of a GAP/CL20/AP composite solid propellant is still very small. In addition, due to the poor convergence of a super-viscous elastic binder matrix under the condition of a large deformation and the existence of cohesive elements between the particles and matrix, research on the micro-mechanical properties of a propellant is still in the stage of small deformations.

Based on the MPM and FEM, the numerical codes of the generating algorithm of CL20 and AP grains in a GAP matrix are compiled in this paper, and a numerical model of the particle/matrix debonding damage evolution process under finite deformation is established and realized. FEM was used to simulate the debonding process and meso-damage evolution law of the interface between the composite solid propellant grains and matrix. Combined with the experiments, the effects of meso-interface characteristics and macro-mechanical particle size are studied. In addition, the meso-failure mechanism of a composite propellant is discussed too. In this paper, it is of great significance to predict the macro-mechanical properties and to analyze the meso-failure mechanism damage evolution process of GAP/CL20/AP composite propellants.

2. The Basic Theory of MPM

MPM uses particles to represent the range of materials, and the particles contain historical variables such as stress, strain, position, speed, and energy. The interaction between particles and the updating of historical variables of particles depends on the background grid [28]. With the continuous development of the algorithm in recent decades [29–42], the MPM has been widely used in numerical calculations of impact penetration, hypervelocity collisions, fluid–solid coupling, explosions, crack propagations, material failures, geotechnical impact failures, etc. [43–52]. Particle position and other information can be easily mapped to the regular background grid, so it is very convenient to find the overlapping information of different parts by using its preprocessing technology.

The control equations followed by the MPM include the mass conservation equation, the momentum conservation equation, and the energy conservation equation, which must be followed in the calculation process of the MPM.

$$\begin{cases} Massconservation\ equation:\ \rho(\mathbf{X},t)J(\mathbf{X},t)=\rho_0(\mathbf{X}) \\ Momentum\ conservation\ equation:\ \sigma_{ij,j}+\rho b_i=\rho\ddot{u}_i \\ energy\ conservation\ equation:\ \rho\dot{w}^{\text{int}}=D_{ij}\sigma_{ij} \end{cases} \tag{1}$$

where $\rho(\mathbf{X},t)$, $J(\mathbf{X},t)$, and $\rho_0(\mathbf{X})$ represent the density of the material at the current moment, the determinant of the deformation gradient, and the density at the initial moment, respectively. D_{ij} and σ_{ij} are the deformation rate tensor and the Cauchy stress tensor. u_i and b_i denote the displacement vector and physical force vector, and w^{int} is the internal energy of the material per unit mass.

In the process of material point method calculation, the integration of the momentum equation and the calculation of a spatial derivative depend on the background grid, and its virtual work equation is as follows:

$$\int_V \delta u_i \rho \ddot{u}_i dV + \int_V \delta u_{i,j}\sigma_{ij}dV - \int_V \delta u_i \rho b_i dV - \int_{\Gamma_t} \delta u_i \bar{t}_i d\Gamma = 0 \tag{2}$$

As shown in Figure 1, after a substance is dispersed into a series of particles, its density can be expressed as follows:

$$\rho = \sum_{p=1}^{N_p} m_p \delta(x - x_p) \tag{3}$$

where x_{ip} and m_p represented the mass and coordinates of the particles, respectively. δ is the Dirac delta function. Formula (3) is substituted into the virtual work of Equation (2) and converted into the form of summation:

$$\sum_{p=1}^{n_p} m_p \ddot{u}_{ip}\delta u_{ip} + \sum_{p=1}^{n_p} m_p \sigma^s_{ijp}\delta u_{ip,j} - \sum_{p=1}^{n_p} m_p b_{ip}\delta u_{ip} - \sum_{p=1}^{n_p} m_p \bar{t}^s_{ip} h^{-1}\delta u_{ip} = 0 \tag{4}$$

where $u_{ip} = u_i(x_p)$, $\delta u_{ip,j} = \delta u_{i,j}(x_p)$, $\sigma^s_{ijp} = \sigma^s_{ij}(x_p)$, and $b_{ip} = b_i(x_p)$, $\bar{t}^s_{ip} = \bar{t}^s_i(x_p)$. h is the thickness of the assumed boundary, the integral term in Formula (2) is converted into a summation term by Formula (4), and the motion equation of the background grid node is as follows:

$$\dot{p}_{iI} = f^{\text{int}}_{iI} + f^{\text{ext}}_{iI}, x_I \notin \Gamma_u \tag{5}$$

$$\dot{p}_{iI} = M_{IJ}\dot{u}_{iJ} \tag{6}$$

$$M_{IJ} = \sum_{p=1}^{n_p} m_p N_{Ip} N_{Jp} \tag{7}$$

where $\dot{p}_{iI}$ represents the momentum of grid nodes I in the direction of i and M_{IJ} is the mass matrix of the background grid.

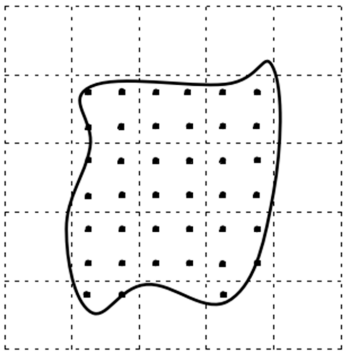
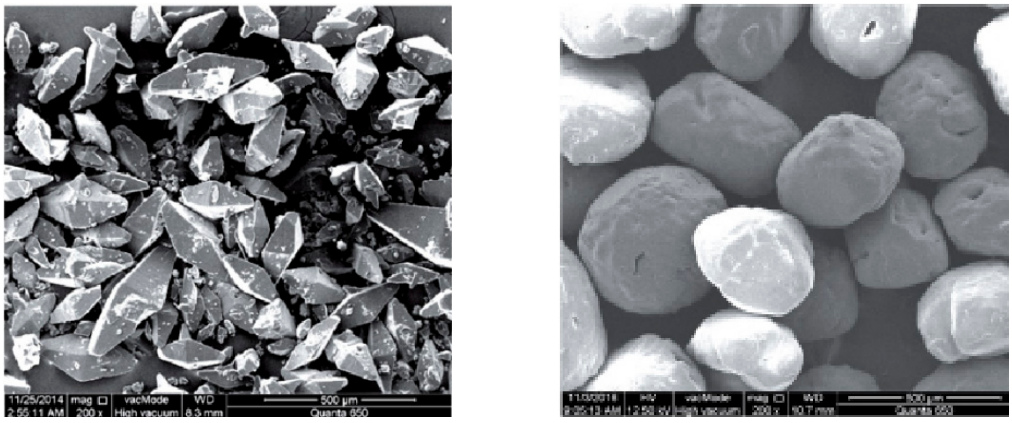


Figure 1. Schematic diagram of material point method.

3. The Modeling Process

This project focuses on a GAP/CL20/AP composite propellant. According to the real grain size of the propellant, the grain size distribution of AP and CL20 obeys normal distribution. The morphology of the grains in a GAP/CL20/AP composite propellant were shown in Figure 2. As shown in Figure 2, the grain size of AP was relatively large and its shape was nearly spherical, whereas the size of CL20 was relatively small, showing a fusiform shape.



(**a**) (**b**)

Figure 2. The morphology of CL20 and AP grains: (**a**) the morphology of CL20 grains; (**b**) the morphology of AP grains.

3.1. Grain Generation Method

This CL20 and AP grain generation method was coded in Fortran language (see Appendix A). At first, from the aspect of grain size generation, random numbers with uniformly distributed grain sizes were directly generated through the random function related to the system clock. Then, the discrete function with normal distribution was generated by combining a Box–Muller algorithm, and the generated grains should be put into the matrix according to the grain size from large to small.

From the aspect of CL20 grain morphology, as shown in Figure 2a, the polygon ABCDEF grain was generated in a local coordinate system, as shown in Figure 3a; then, the polygon grain was discretized into particles. In the local coordinate system, one red particle $P(x', y')$ was chosen. If the point P rotates around the point O by a random angle θ, the new coordinates of the particle can be obtained as follows:

$$\begin{cases} x = x' \cos\theta - y' \sin\theta \\ y = x' \sin\theta + y' \cos\theta \end{cases} \tag{8}$$

Considering the mirror and move operations of grains in the matrix, Equation (8) would be as follows:

$$\begin{cases} x = \eta x' \cos\theta - y' \sin\theta + x_m \\ y = \eta x' \sin\theta + y' \cos\theta + y_m \end{cases} \tag{9}$$

where the probability of mirror operations parameter $\eta = 1$ and $\eta = -1$ is 50%, and (x_0, y_0) is the translation distance of the grain center O in the local coordinate system.

From the aspect of AP grain morphology, as shown in Figure 2b, the rounded grain was generated in a local coordinate system, as shown in Figure 3b; then, the polygon grain was discretized into particles. Considering the movement operations of grains in the matrix, the equation would be as follows:

$$\begin{cases} x = x' + x_m \\ y = y' + y_m \end{cases} \tag{10}$$

where (x', y') is the original coordinate in the local coordinate system, and (x_m, y_m) is the translation distance of the grain center O in the local coordinate system.

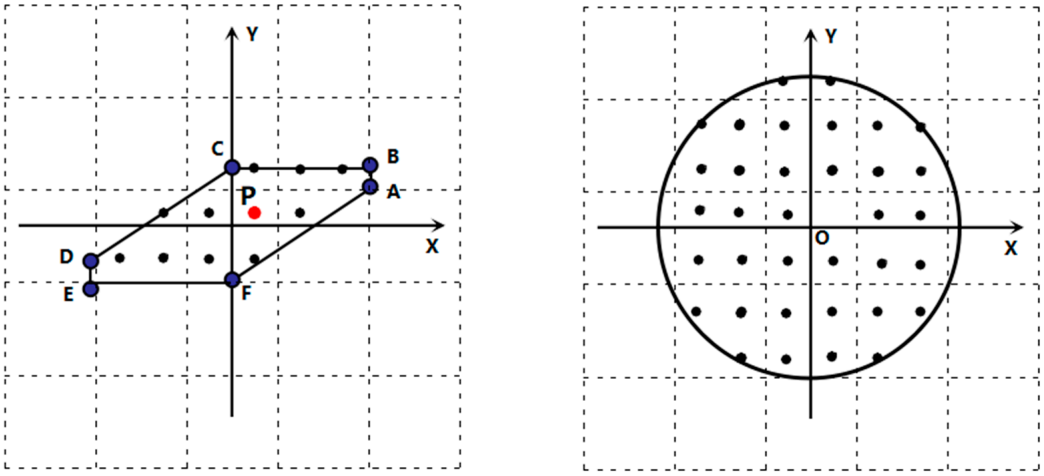


Figure 3. Two-dimensional grain dispersion in propellant: (**a**) dispersion of CL20 grain, the red particle P is randomly selected; (**b**) dispersion of AP grain.

3.2. The Uniform Displacement Boundary Conditions

In order to simulate the debonding process between the grains and matrix of a GAP/CL20/AP propellant under uniaxial constant tension, the established mesoscopic model was numerically simulated with reasonable boundary conditions. As shown in Figure 4, Figure 4a,b,d have a fixed restraint load on the lower boundary and an upper boundary as the load bearing end. The left boundary and the right boundary of Figure 4a are unconstrained boundaries; Figure 4b shows that the left boundary and the right boundary are vertical boundaries, that is, the boundaries were kept vertical during deformation. The left boundary and the right boundary of Figure 4d are periodic boundaries. The upper, lower, left, and right boundaries of Figure 4c are all periodic boundaries. Generally, it is considered that a representative volume unit is representative when its size is 3–5 times the maximum grain size [53]. In this project, the grain distribution is non-periodic, so the uniform displacement boundary condition in Figure 4b is selected for numerical calculation.

3.3. The Establishment of Micro-Finite Element Calculation Model of Propellant

Based on the MPM, the generated AP particles and CL20 grains were imported into the commercial software Abaqus through python scripting codes for numerical calculation. The cohesion elements with zero thickness were inserted between the grains and matrix (as shown in Figure 5b). Since the bilinear cohesion element was simple and the model parameters were easy to obtain, the bilinear cohesion element was adopted in this project.

In this project, 1000 μm × 600 μm is selected as the size of a representative volume unit. Table 1 shows the ingredient contents of the AP and CL20 grains. The sizes of the AP grains conform to the normal distribution, with a distribution range of 50~280 μm and an average value of 140 μm. Additionally, the sizes of the CL20 grains conform to the normal distribution, with a distribution range of 20~90 μm and an average value of 50 μm. The grain filling fraction of the composite solid propellant is shown in Table 1. The propellants in this paper are all of this formula.

Since it was difficult to observe the debonding of tiny grains such as aluminum grains during the deformation of a propellant, in order to establish the numerical model conveniently and to avoid the difficulty of model convergence caused by too dense grids, Al grains and other liquid components were generally classified as an adhesive matrix.

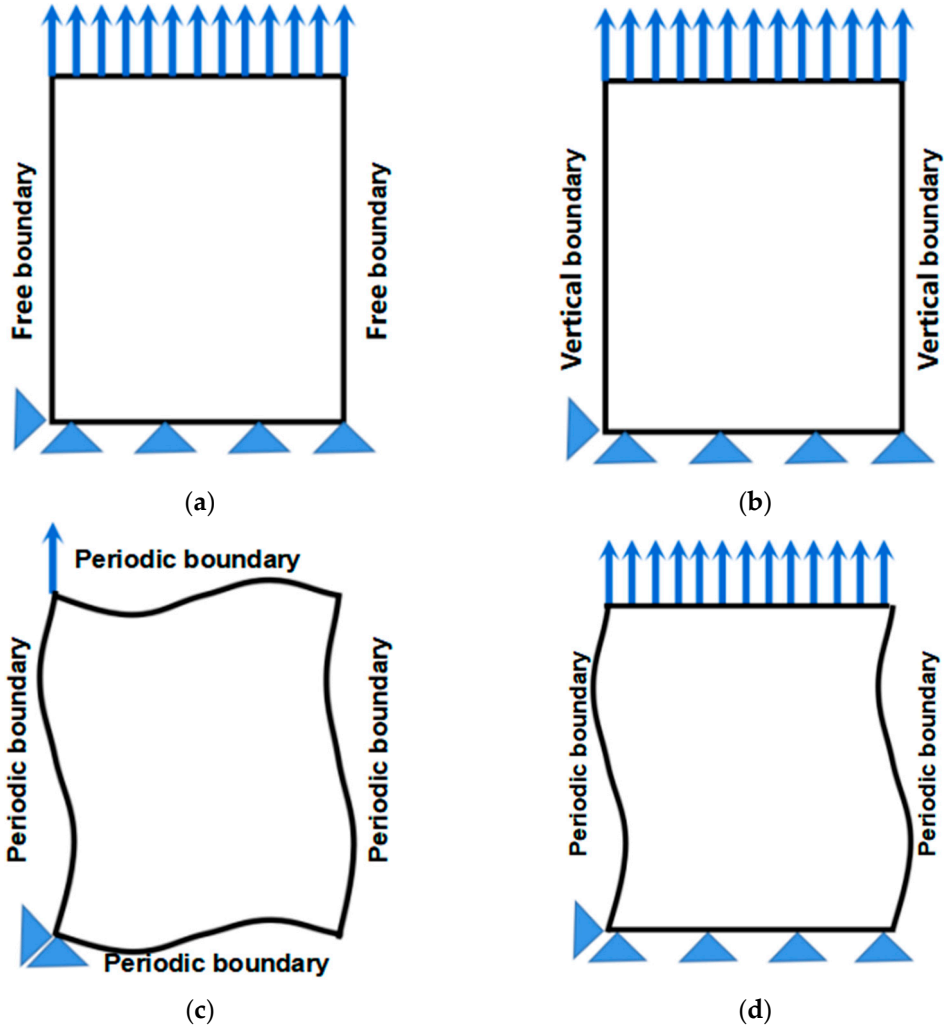


Figure 4. The commonly used boundary conditions: (**a**) free boundary condition; (**b**) uniform displacement boundary condition; (**c**) periodic axisymmetric boundary condition; (**d**) periodic boundary condition.

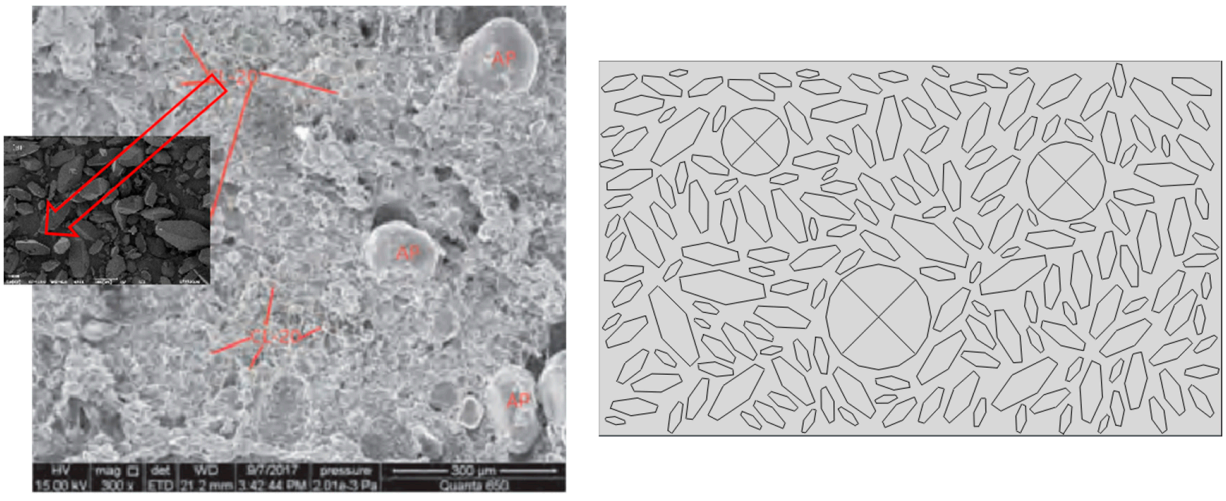


Figure 5. (**a**) Mesoscopic photograph of GAP/AP/CL20 propellant; (**b**) Meso-numerical model of GAP/AP/CL20 propellant.

Table 1. The content and size distribution of various components of the propellant.

Component	AP	CL20	Al, Plasticizer, etc.
Mass fraction/%	9.58	40.13	50.29
Volume fraction/%	8.95	34.18	56.87
Grain size/um	50–280 normal distribution	20–90 normal distribution	Classified as adhesive matrix

3.4. The Constitutive Model of Grains and Matrix

Compared with polymer adhesives, the elastic modulus of AP and CL20 grains is very large, the constitutive model of their materials can be approximately considered as linear elasticity, and the plane stress CPE4 element is selected. The mechanical properties elastic modulus E and Poisson's ratio v of the Cl20 and AP grains are shown in Table 2.

Table 2. Mechanical properties of Cl20 and AP grains [54,55].

Component	E(GPa)	v
CL20 grains	17.1	0.2
AP grains	32,450	0.14

Other small grains and the binder matrix GAP could be considered as a homogeneous hyperelastic mixture matrix, and the hyperelastic constitutive model above the second order has a high accuracy. Furthermore, the viscoelastic properties of a mixed matrix under dynamic loads such as large deformation, long-time loading, impact, or cyclic loading can not be ignored, so a viscoelastic and hyperelastic constitutive model should be established, and the stress expression of this model is as follows:

$$\sigma = \sigma^e + \sigma^v \tag{11}$$

where σ^e denotes the viscoelastic part and σ^v represents the hyperelastic part. The second-order simplified polynomial model is stable in all strain ranges and has high accuracy, so this paper chooses the second-order simplified polynomial model as the constitutive model of the hyperelastic part of a GAP adhesive. The form of the reduced polynomial strain energy potential is as follows:

$$U = \sum_{i=1}^{N} C_{i0}(\bar{I}_1 - 3)^i + \sum_{i=1}^{N} \frac{1}{D_i}(J-1)^{2i} \tag{12}$$

where U is the strain energy per unit of reference volume; N is a material parameter; C_{i0} and D_i are temperature-dependent material parameters; and $\bar{I}_1$ is the first deviatoric strain invariant. The stress expression of the hyperelastic part is as follows:

$$\sigma^e = \sum_{n=1}^{2} \frac{2\mu_n}{\alpha_n}\left(\lambda^{a_n-1} - \lambda^{-a_n/2-1}\right) \tag{13}$$

The viscoelastic part is a second-order Prony model, and its stress expression is as follows:

$$\sigma^{\mathrm{v}} = \int_0^t \sum_{m=1}^{2} E_m \exp\left(-\frac{t-\tau}{\tau_m}\right)\frac{\partial \varepsilon}{\partial \tau}\mathrm{d}\tau \tag{14}$$

In this paper, the parameters of second-order simplified polynomial hyperelastic and second-order viscoelastic materials were obtained according to Reference [2], as shown in Table 3:

Table 3. Mechanical property parameters of second-order hyperelastic and viscoelastic materials.

C_{10}	C_{01}	C_{20}	C_{11}	C_{02}	D_1	D_2
0.1481	0	0.011527	0	0	0	0
E_1	τ_1	E_2	τ_2			
0.06217	28.2648	0.02364	394.0152			

3.5. Interface Model of Binder/Grain

According to the experimental results of the propellant, there was an obvious interface between binder and solid grains, and the interfacial debonding was one of its main damage modes [11]. Generally, cohesive elements can be used to model the interfacial debonding process [13,14]. The bilinear model of the cohesive element is adopted in this project because of its simple structure and easy acquisition of the parameters. The traction-displacement laws of the normal direction n and the tangent directions t and n of the interface satisfy the following:

$$\begin{aligned} T_n &= K(1-D)\delta_n \\ T_t &= K(1-D)\delta_t \\ T_s &= K(1-D)\delta_s \end{aligned} \tag{15}$$

where K is the initial interface stiffness; $\delta_n, \delta_t, \delta_s$ denote the displacement component; T_n, T_t, T_s represent the stress component; and the damage factor D is as follows:

$$D = \begin{cases} 0, & \delta \le \delta^0 \\ \frac{\delta^f(\delta-\delta^0)}{\delta(\delta^f-\delta^0)}, & \delta > \delta^0 \end{cases} \tag{16}$$

where T_c is the maximum fracture stress, δ^0 denotes the critical opening displacement of the interface, δ represents the opening displacement, and δ^f is interface failure displacement. In addition, this project used the MAXS fracture criterion to describe the damage evolution of cohesive elements.

$$\max\left\{\frac{\langle T_n\rangle}{T_n^c}, \frac{T_s}{T_s^c}, \frac{T_t}{T_t^c}\right\} = 1 \tag{17}$$

where T_n^c, T_s^c, T_t^c represent the peak values of the nominal stress when the deformation is either purely normal to the interface or purely in the first or the second shear direction, respectively. The bilinear model of cohesive elements in the commercial software Abaqus mainly includes three parameters: K, T_c, δ^f. Since the interface parameters between the micro-particles of the propellant and the binder matrix could not be obtained directly by experiments but the exact value of the parameters needs to be obtained, an inverse analysis method was adopted to solve the parameters by using the experimental results such as the macroscopic stress–strain curve. This method needs to constantly adjust the parameters in the numerical simulation to achieve a good agreement between the numerical simulation and the experimental results. Additionally, the adjusted parameter values are regarded as accurate values of the parameters. In recent years, the inverse analysis method has been widely used in many fields such as structural optimization and material parameter identification. In this paper, the experimental stress–strain curve is expressed as a set of a certain number of points:

$$F(x) = (x_i, F(x_i))\ i = 1, 2, 3, \cdots, n \tag{18}$$

Next, the stress–strain curve calculated by Abaqus is also expressed as a set of n points:

$$Q(x) = (x_i, Q(x_i))\ i = 1, 2, 3, \cdots, n \tag{19}$$

The objective interpolation function, which can reflect the closeness between experiment and numerical simulation, is expressed as follows:

$$\min R = \frac{1}{n}\sum_{i=1}^{n}[F(x_i) - Q(x_i)]^2 \; i = 1, 2, 3, \cdots, n \tag{20}$$

where n is the number of evenly distributed discrete points, i represents the i-th point, $F(x_i)$ denotes the experimental result value of the i-th point, and $Q(x_i)$ is the simulation result of the i-th point. The number of discrete points selected in this paper is 34. At present, due to the lack of experimental methods to obtain these parameters and considering the close mechanical properties of the interface between AP and CL20, the idea of an inverse was adopted in this study to finally determine the values of the interface parameters K, T_c, δ^f, which are 683 MPa/mm, 1.113 MPa, and 0.211 mm, respectively [2].

In this paper, the calculation processes of the material point method and the finite element method are shown in the following Figure 6:

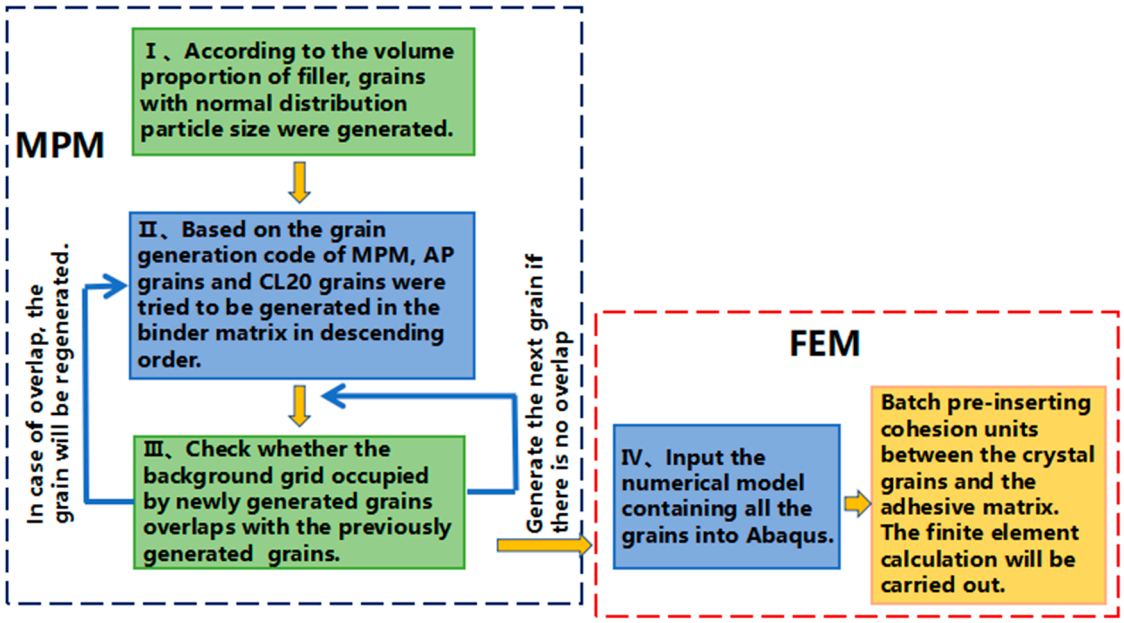


Figure 6. Stress–strain curve of GAP/CL20/AP propellant.

4. Simulation Results and Discussion

In this paper, the mechanical behavior of a representative volume unit of the propellant under a uniaxial tensile load of 100 mm/min at 20 °C was numerically simulated. At first, the MPM program written in Fortran code was used to generate the initial mesoscopic model of the composite propellant; this process took about 15 min. Secondly, the positions of the grains in which distorted meshes were easy to generate were properly adjusted, and the adjusted model was written into a python script file and imported into Abaqus, the commercial finite element software. Using Abaqus, the commercial finite element software, this example ran on a high-performance computer with 16 cores and 64G memory for 10 h to complete the calculation. The uniaxial tensile time simulated in this project was 33.049 s, and the specific numerical simulation results were written as follows:

4.1. Debonding Process of AP Grains and CL20 Grains

A numerical simulation of the uniaxial tension of the meso-model was carried out using the commercial finite element software Abaqus, and Figure 7 shows the stress nephograms corresponding to propellant strains of 30%, 60% and 80%.

In this paper, the model was established according to the true composition and grain arrangement morphology of the propellant. As shown in Figure 7, during the initial stage of the uniaxial tensile nominal strain reaching 30%, the bonding interface between grain substrates was well bonded. Because the modulus of the grains was much higher than

that of the matrix, stress concentration mainly occurs in the interior of the grains and in the matrix of adjacent grains. As the nominal strain reaches 60%, debonding occurs first in the vicinity of large grains and then in dense grain areas. The reason for this is that the strain of the matrix is large near large grains and dense grain areas, which become weak links in the propellant, and these areas are prone to interfacial debonding. As the nominal strain reached 80%, at this time, much interfacial debonding occurred, which led to the gradual convergence of micro-cracks, which eventually tore the matrix and caused the macro-destruction of the propellant. This was consistent with the conclusions in Reference [56].

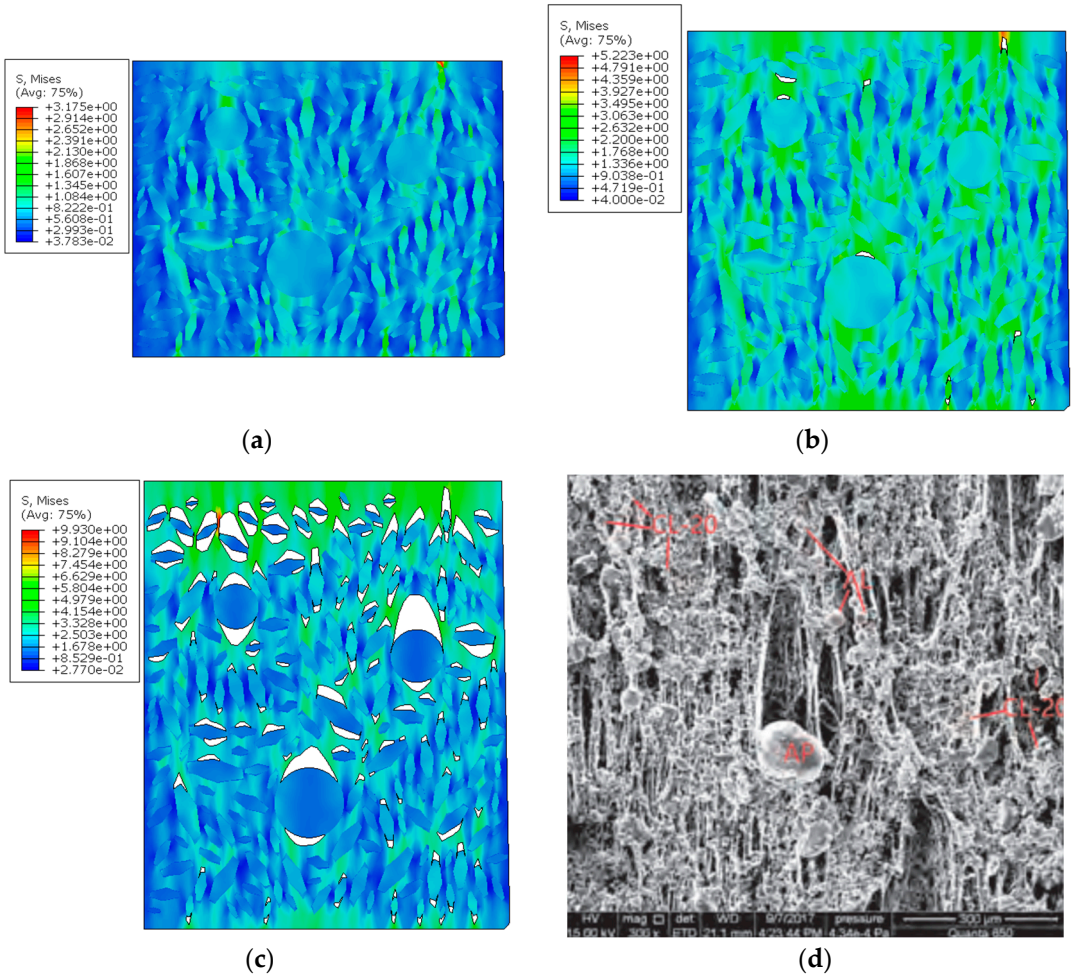


Figure 7. The stress nephogram of propellant under different strains: (**a**) At a strain value of 3×10^{-2}; (**b**) At a strain value of 6×10^{-2}; (**c**) At a strain value of 8×10^{-2}; (**d**) The scanning electron microscope of the propellant before tensile fracture [7].

Figure 8 shows the engineering stress–strain curve of the composite propellant at a 100 mm/s tensile rate, wherein the black curve is the curve obtained by numerical simulation, and the curves of the other three colors were obtained from experiments. As shown in Figure 8, when the strain is small ($\varepsilon < 30\%$), the propellant is in the linear elastic region, and the stress increases linearly with the increase in strain. When the strain reaches 60%, the interfacial adhesion strength becomes weak, and the stress–strain curve begins to appear nonlinear. When the load continues to increase to a strain of 80%, there is more debonding at the particle interfaces, and the stress hardly increases with the increase in strain. Comparing the simulation curve of the meso-model in Figure 8 with the macro-experimental curve of this propellant, it can be seen that after inversion analysis, the simulation curve is basically consistent with the real experimental curve, the value of

the objective interpolation function min$R$ in Equation (20) is 0.05078%, and the degree of coincidence is very high in the strain range of 20–80%, so it can be considered that the simulation results can reflect a real experiment.

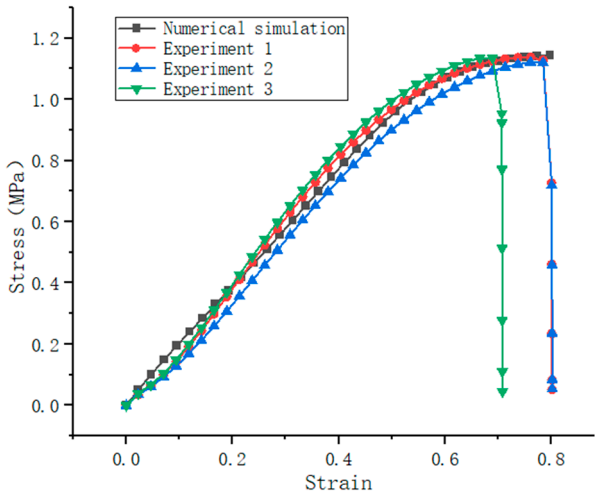


Figure 8. Stress–strain curve of GAP/CL20/AP propellant.

We thought the reasons for the gap were as follows: (1) The micro-simulation of the propellant in this paper was based on two-dimensional plane strain, which had some deviation from the three-dimensional one; (2) the initial microscopic defects such as micropores, microcracks, and incomplete grain wrapping were not considered when establishing the microscopic model. The initial microscopic defects will lead to a decrease in the initial modulus.

4.2. Effect of Interface Parameters on Macromechanical Properties

The study of different interface parameter models shows that the three related parameters K, T_c, δ^f in the interface model have significant influence on the mechanical properties of the propellant. By changing the interface parameters, the changes in the nominal stress–strain relationship curve are as follows:

As shown in Figure 9a, when the initial stiffness K decreased from 683 MPa·mm^{-1} to 383 MPa·mm^{-1}, the initial elastic modulus E of the propellant decreased from 2.214966 MPa to 2.039941 MPa, which reduced to the previous 92.0981%. When the initial stiffness K increased from 683 MPa·mm^{-1} to 983 MPa·mm^{-1}, the initial elastic modulus E of the propellant increased from 2.214966 MPa to 2.0966 MPa, which up to the previous 103.8132%. It can be seen that with the increase in initial stiffness K, the elastic modulus E of propellant increases gradually, but the growth rate becomes slower and slower. However, the parameter K has little influence on the peak value of nominal stress. As mentioned above, the initial interface stiffness K mainly determines the slope of the linear rising section of the stress–strain curve, and the increase in the initial interface stiffness K makes the stress increase rapidly in the early stage.

As shown in Figure 9b, when the maximum fracture stress T_c decreased from 1.113 MPa to 0.613 MPa, the maximum stress σ_{max} of the propellant decreased from 1.143782 MPa to 0.703362 MPa, which reduced to the previous 61.4944%. When the maximum fracture stress T_c increased from 1.113 MPa to 1.613 MPa, the maximum stress σ_{max} of the propellant increased from 1.143782 MPa to 1.485626 MPa, which up to the previous 129.8872%. It can be seen that with the increase in initial stiffness T_c, the maximum stress σ_{max} of the propellant increases. As mentioned above, the maximum fracture stress T_c mainly affects the peak value of the stress and determines the basic trend of the stress–strain curve. With the increase in the maximum fracture stress T_c, the stress value increases.

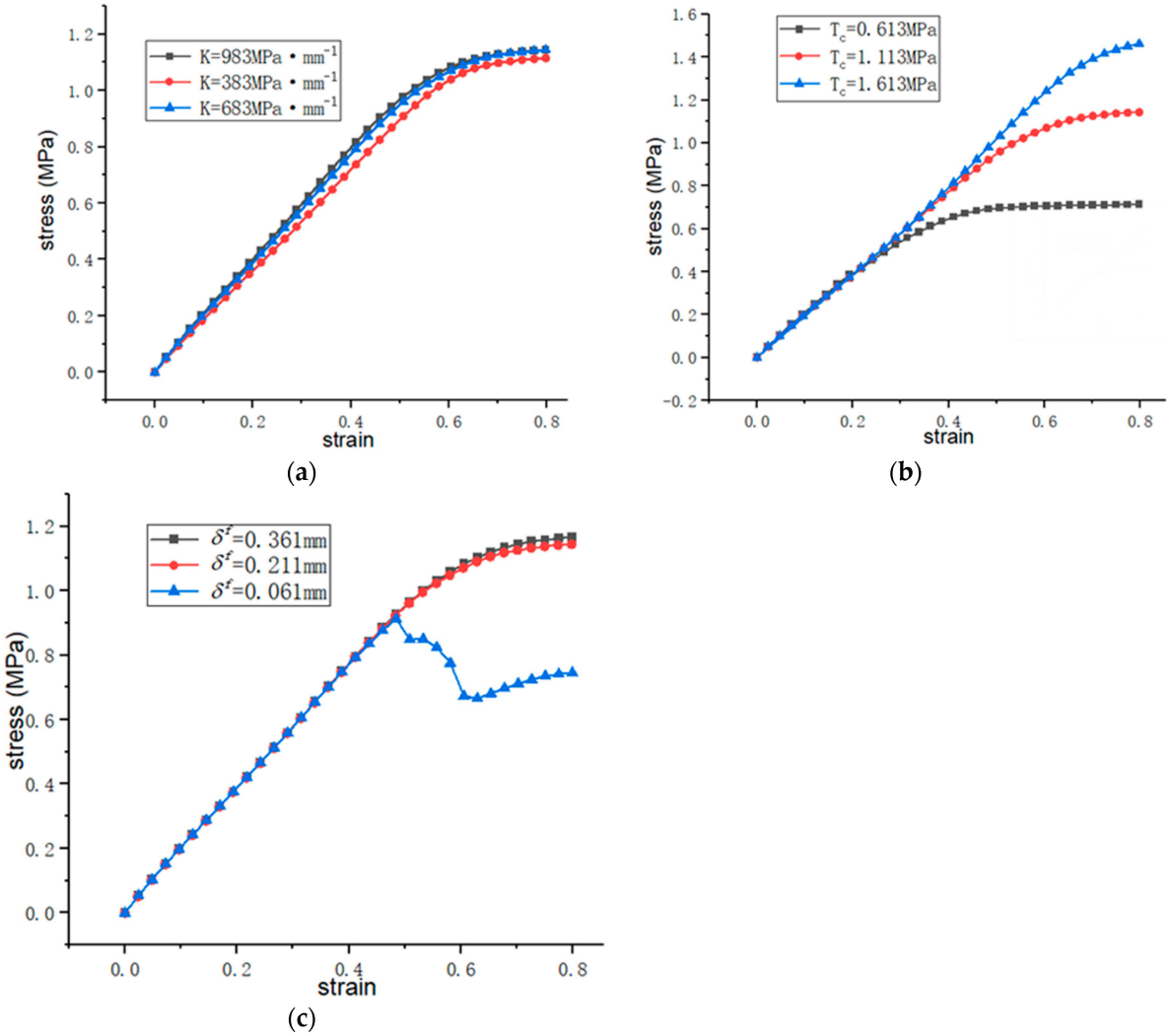


Figure 9. Effect of interface parameters on the stress–strain curve. (**a**) The stress–strain curves under different parameters K; (**b**) the stress–strain curves under different parameters T_c; (**c**) the stress–strain curves under different parameters δ^f.

As shown in Figure 9c, when the interface failure displacement δ^f decreased from 0.211 mm to 0.061 mm, the maximum stress σ_{max} of the propellant decreased from 1.143782 MPa to 0.913491 MPa, which reduced to the previous 79.8658%. When the interface failure displacement δ^f increased from 0.211 mm to 0.361 mm, the maximum stress σ_{max} of the propellant increased from 1.143782 MPa to 1.1661 MPa, which up to the previous 101.9512%. It can be seen that the interface failure displacement δ^f mainly affects the damage softening section of the stress–strain curve. In the damage softening stage, the greater the interface failure displacement δ^f, the slower the stress decreases with the strain. If the failure displacement is too small, even in the case of a small strain, the interfaces are destroyed and lose their bearing capacity, and the stress in the model drops sharply (as shown by the blue curve in Figure 9c).

5. Conclusions

When the GAP/CL20/AP composite solid propellant was subjected to an external load, micro-cracks, micro-hole expansion, and local stress concentration may destroy the microstructure of interface bonding, thus affecting its macro-mechanical properties. Based on the advantages of the material point method and the finite element method, this paper systematically carried out a meso-damage experiment on the composite propel-

lant and a numerical simulation study of its mechanical behavior, mainly including the following contents:

(1) In this paper, the microstructure model of a GAP/CL20/AP composite solid propellant was established based on the MPM. The developed Fortran codes are suitable for generating grains with arbitrary shapes, such as CL20 and AP grains. The grains are generated in order from largest to smallest. The minimum distance between the generated grains can be controlled by adjusting the size of the background grid. The filling ratio of grains can meet the requirements of the grain proportion in a real propellant. In this paper, it takes about 15 min to generate grains in this numerical model. Therefore, it shows that the numerical model generated by this method is efficient. The generated AP and CL20 grains are imported into the commercial software Abaqus through python scripting codes for numerical calculation.

(2) In this paper, a numerical simulation of the uniaxial tension of the meso-model was carried out using the commercial finite element software Abaqus. The evolution process of interface damage between CL20 grains and AP grains, and the GAP adhesive matrix thus becomes clear. Furthermore, the relationship between meso-damage and the macro-stress–strain curve is clearly expressed. During the initial stage of the uniaxial tensile nominal strain reaching 30%, the bonding interface between grain substrates is well bonded. The propellant is in the linear elastic region. As the nominal strain reaches 60%, debonding occurs first in the vicinity of large grains and dense grain areas, and the stress–strain curve begins to appear nonlinear. As the nominal strain reached 80%, a large number of interfacial debonding occurred, and the stress hardly increased with the increase in strain. It can be considered that the simulation results can reflect a real experiment.

(3) The study of different interface parameter models shows that the three related parameters K, T_c, δ^f in the interface model have significant influence on the mechanical properties of the propellant. The initial interface stiffness K mainly determines the slope of the linear rising section of the stress–strain curve. The maximum fracture stress T_c mainly affects the peak value of the stress. The interface failure displacement δ^f mainly affects the damage softening section of the stress–strain curve.

According to the research above, it can be seen that the macroscopic mechanical properties of a GAP/CL20/AP propellant strongly depend on the evolution of its microstructure. However, the micro-numerical simulation of propellants is not perfect, such as the establishment of a three-dimensional micro-model. In the micro-finite element calculation, it is considered that the main factor of composite propellant damage is the debonding of the particle–matrix interface. In fact, the internal microstructure of composite propellants is very complicated during storage and transportation, and the interface damage is only one important factor. Other factors, such as damage and tear of the binder matrix, need to be fully considered in a follow-up study. In order to prevent micro-debonding, researchers and engineers need to change the chemical properties of the bonding interface, such as changing the chemical properties of the adhesive and adding other additives to the propellant, so much work still needs to be carried out in the future.

Author Contributions: X.G. wrote the Fortran and python codes and wrote the original draft; X.L. provided the experimental funds and experimental conditions; C.D. guided the formula derivation and program debugging; G.Z. collected the experimental data; L.Z. assisted in debugging the programs; F.Z. used Abaqus for the modeling. All authors have read and agreed to the published version of the manuscript.

Funding: This research was funded by Beijing Institute of Technology. grant number [2023410404000009].

Institutional Review Board Statement: The study was conducted in accordance with the Declaration of Helsinki, and approved by the Institutional Review Board.

Informed Consent Statement: Informed consent was obtained from all subjects involved in the study.

Data Availability Statement: Because of confidentiality, the sources of some data about the propellants in this paper are not provided.

Conflicts of Interest: The authors declare no conflict of interest.

Appendix A

Algorithm A1 The CL20 and AP grain generation method coded in Fortran language

```
    parCounter = 1
    bvolume_ = 0.0d0
    n1_ = 0 !big AP
    n2_ = 0 !small CL20
    mj1_ = 0.0d0
    mj2_ = 0.0d0
    totmj_ = (SpanX(2)-SpanX(1))*(SpanY(2)-SpanY(1))

          call random_seed () !@
!!!!!!!!big AP
               dfnum_=.true.
          do while(dfnum_)
                call random_number(×1_)
                call random_number(×2_)
                r1_= sqrt(-2.0*log(×1_))*cos(2.0*3.1415926d0*×2_)
                     if(r1_<-3.0d0 .or.r1_>3.0d0) cycle
                r1_= 0.075d0+0.075d0*(r1_)/3.0d0
                     if(r1_<=0.015d0) cycle
                mj1_ = mj1_ + 3.1415926*r1_**2.0d0/totmj_

                    if(mj1_<0.093627d0) then    !!!!!!!normal number 0.10d0
                !     if(n1_<3) then!!!!!!little number correct@@@@@@@@@@@@
                        dfnum_=.true.
                      else
                        dfnum_=.false.
                      end if
                      if(dfnum_==.false.) cycle !exit
                        n1_ = n1_ + 1

             if(n1_==1)then
                    allocate(big_AP(n1_))
                    big_AP(n1_) = r1_
                    allocate(cha_AP(n1_))
             else
                    deallocate(cha_AP)
                    allocate(cha_AP(n1_))

                     paid_ = .false.
                do i = 1, n1_-1
                    if(big_AP(i) >= r1_)then
                    cha_AP(i) = big_AP(i)
                    else
                    cha_AP(i) = r1_
                    cha_AP(i+1:n1_) = big_AP(i:n1_-1)
                      paid_ = .true.
                    end if

                    if(i==n1_-1 .and. paid_ ==.false.)then
                       cha_AP(n1_) = r1_
```

```
                end if

                if(paid_) exit
            end do

                deallocate(big_AP)
                allocate(big_AP(n1_))
                big_AP = cha_AP
        end if
    end do
    write(*,*) "AP",n1_,big_AP !
!!!!!!!!!!!!!!!!!!!!!

    !!!!!!!!!!!!!!!!!!!!small CL20
        dfnum_=.true.
    do while(dfnum_)
            c_ = 0
            call random_number(×3_)
            call random_number(×4_)
            r2_= sqrt(-2.0*log(×3_))*sin(2.0*3.1415926d0*×4_)
                if(r2_<-3.0d0 .or.r2_>3.0d0) cycle

            r2_= 0.02d0+0.03d0*(r2_)/3.0d0
                if(r2_<=0.005d0) cycle
            mj2_ = mj2_ + 2.75d0*2.3094d0*r2_*r2_/totmj_/2.5166d0/2.5166d0
             !write(*,*) "aaaaa1",r2_,mj2_
                if(mj2_<0.369212d0) then    !0.369212d0
                dfnum_=.true.
              else
                dfnum_=.false.
              end if
              if(dfnum_==.false.) cycle !exit
            n2_ = n2_ + 1
      if(n2_==1)then
            allocate(sma_CL20(n2_))
            sma_CL20(n2_) = r2_
            deallocate(cha_AP)!!!!!!!!!!!
            allocate(cha_AP(n2_))
      else
            deallocate(cha_AP)
            allocate(cha_AP(n2_))

            paid_ = .false.
       do i = 1, n2_-1
          if(sma_CL20(i) >= r2_)then
          cha_AP(i) = sma_CL20(i)
          else
          cha_AP(i) = r2_
          cha_AP(i+1:n2_) = sma_CL20(i:n2_-1)
            paid_ = .true.
          end if

          if(i==n2_-1 .and. paid_ ==.false.)then
             cha_AP(n2_) = r2_
          end if
```

```
                    if(paid_) exit
            end do

                deallocate(sma_CL20)
                allocate(sma_CL20(n2_))
                sma_CL20 = cha_AP
          end if
      end do
            write(*,*) "small CL20",n2_,sma_CL20

!!!!!!!!!!end small
```

References

1. Li, S.W.; Zhao, F.Q.; Yuan, C.; Luo, Y.; Gao, Y. Research trend of solid propellants abroad. *J. Solid Rocket Technol.* **2002**, *25*, 36–42.
2. Feng, T. Numerical Simulation of Meso-Mechanics Damage in Composite Solid Propellant Based on Mesoscopic Model. Ph.D. Thesis, Nanjing University of Science & Technology, Nanjing, China, 2017.
3. Liu, X.G.; Liu, P.J.; Qiang, H.F.; Zhang, Y. Quantificational method of debonding damage of HTPB propellant based on micro-CT detection. *J. Propuls. Technol.* **2019**, *40*, 1162–1168.
4. Gao, H.; Liu, H.; Qi, Z.; Liu, H.; Zheng, H. Research on variation law of fatigue crack-tip displacement and strain fields based on high-speed digital image correlation method. *Acta Arrnamentarii* **2015**, *36*, 1772–1781.
5. Cui, H.R.; Li, H.Y.; Shen, Z.B. Cohesive zone model for mode-I fracture with viscoelastic-sensitivity. *Eng. Fract. Mech.* **2019**, *221*, 106578.
6. Zhang, L.; Zhi, S.; Shen, Z. Research on tensile mechanical properties and damage mechanism of composite solid propellants. *Propellants Explos. Pyrotech.* **2018**, *43*, 234–240. [CrossRef]
7. Zhou, S.; Tang, G.; Pang, A.; Xu, H.; Song, H. Evolution of meso-structure of GAP composite solid propellants. *J. Solid Rocket Technol.* **2018**, *41*, 580–585 and 592.
8. Chen, Y.; Liu, Y.; Xia, J.; Tan, H. Numerical simulation of stress distribution and analysis of damage trend of NEPE propellants. *Chin. J. Energetic Mater.* **2009**, *17*, 87–90.
9. Matouš, K.; Inglis, H.M.; Gu, X.; Rypl, D.; Jackson, T.L.; Geubelle, P.H. Multiscale modeling of solid propellants: From particle packing to failure. *Compos. Sci. Technol.* **2007**, *67*, 1694–1708. [CrossRef]
10. Inglis, H.M. Modeling the Effect of Debonding on the Constitutive Response of Heterogeneous Materials. Ph.D. Thesis, University of Illinois at Urbana-Champaign, Urbana-Champaign, IL, USA, 2014.
11. Rae, P.J.; Goldrein, H.T.; Palmer, S.J.P.; Field, J.E.; Lewis, A.L. Quasi-static studies of the deformation and failure of β-HMX based polymer bonded explosives. *Proc. Math. Phys. Eng. Sci.* **2002**, *458*, 743–762. [CrossRef]
12. Chang, W.J. Research on Microstructural Damage and Its Numerical Simulation Method for Composite Solid Propellant. Master's Thesis, Nanjing University of Science and Technology, Nanjing, China, 2013. (In Chinese).
13. Li, G.; Wang, Y.; Jiang, A.; Yang, M.; Li, J. Micromechanical Investigation of Debonding Processes in Composite Solid Propellants. *Propellants Explos. Pyrotech.* **2017**, *43*, 642–649. [CrossRef]
14. Zhi, S.-J.; Sun, B.; Zhang, J.-W. Multiscale modeling of heterogeneous propellants from particle packing to grain failure using a surface-based cohesive approach. *Acta Mech. Sin.* **2012**, *28*, 746–759. [CrossRef]
15. Feng, T.; Zheng, J.; Xu, J.; Han, L.; Kang, N. Mesoscopic structure modeling and numerical simulation of debonding process of composite solid propellants. *J. Aerosp. Power* **2018**, *33*, 223–231. (In Chinese)
16. Chang, W.; Ju, Y.; Han, B.; Hu, S.; Wang, Z. Numerical Simulation of Particle/Matrix Interface Failure in Composite Propellant. *J. China Ordnance* **2012**, *8*, 146–153.
17. De Francqueville, F.; Diani, J.; Gilormini, P.; Vandenbroucke, A. Use of a micromechanical approach to understand the mechanical behavior of solid propellants. *Mech. Mater.* **2021**, *153*, 103656. [CrossRef]
18. De Francqueville, F.; Gilormini, P.; Diani, J.; Vandenbroucke, A. Comparison of the finite strain macroscopic behavior and local damage of a soft matrix highly reinforced by spherical or polyhedral particles. *J. Mech.-A/Solids* **2020**, *84*, 104070. [CrossRef]
19. Hu, R.; Prakash, C.; Tomar, V.; Harr, M.; Gunduz, I.E.; Oskay, C. Experimentally-validated mesoscale modeling of the coupled mechanical–thermal response of AP–HTPB energetic material under dynamic loading. *Int. J. Fract.* **2016**, *203*, 1–22. [CrossRef]
20. Prakash, C.; Gunduz, I.E.; Oskay, C.; Tomar, V. Effect of interface chemistry and strain rate on particle-matrix delamination in an energetic material. *Eng. Fract. Mech.* **2018**, *191*, 46–64. [CrossRef]
21. Prakash, C. Effect of Interface Chemical Composition on the High Strain Rate Dependent Mechanical Behavior of an Energetic Material. Ph.D. Thesis, Purdue University Graduate School, West Lafayette, IN, USA, 2019.
22. Matouš, K.; Geubelle, P.H. Finite element formulation for modeling particle debonding in reinforced elastomers subjected to finite deformations. *Comput. Methods Appl. Mech. Eng.* **2006**, *196*, 620–633. [CrossRef]
23. Ngo, D.; Park, K.; Paulino, G.H.; Huang, Y. On the constitutive relation of materials with microstructure using a potential-based cohesive model for interface interaction. *Eng. Fract. Mech.* **2010**, *77*, 1153–1174. [CrossRef]

24. Toulemonde, P.A.; Diani, J.; Gilormini, P.; Desgardin, N. On the account of a cohesive interface for modeling the behavior until break of highly filled elastomers. *Mech. Mater.* **2016**, *93*, 124–133. [CrossRef]
25. Yuan, S.; Tang, W.; Li, G. Analysis on Micro-Mechanical failure Mechanism of Composite Propellant. *J. Solid Rocket Technol.* **2006**, *29*, 48–51.
26. Inglis, H.M.; Geubelle, P.H.; Matouš, K.; Tan, H.; Huang, Y. Cohesive modeling of dewetting in particulate composites: Micromechanics vs. multiscale finite element analysis. *Mech. Mater.* **2007**, *39*, 580–595. [CrossRef]
27. Han, L.; Chen, X.; Xu, J.; Zhou, C.; Zhao, L. Relaxation behavior of composite propellant based on meso-mechanical model. *J. Solid Rocket Technol.* **2017**, *40*, 52–59.
28. Lian, Y. An Adaptive Material Point Finite Element Method and Its Application in Impact/Penetration Problems. Ph.D. Thesis, Tsinghua University, Beijing, China, 2012.
29. Sulsky, D.; Kaul, A. Implicit dynamic in the material-point-method. *Comput. Methods Appl. Mech. Eng.* **2004**, *193*, 1137–1170. [CrossRef]
30. Cummins, S.J.; Brackbill, J.U. An implicit particle-in-cell method for granular materials. *J. Comput. Phys.* **2002**, *180*, 506–548. [CrossRef]
31. Bardenhagen, S.G.; Kober, E.M. The generalized interpolation material point method. *CMES-Comput. Model. Eng. Sci.* **2004**, *5*, 477–495.
32. Wallstedt, P.C.; Guilkey, J.E. An evaluation of explicit time integration schemes for use with the generalized interpolation material point method. *J. Comput. Phys.* **2008**, *227*, 9628–9642. [CrossRef]
33. Zhang, D.Z.; Ma, X.; Giguere, P.T. Material point method enhanced by modified gradient of shape function. *J. Comput. Phys.* **2011**, *230*, 6379–6398. [CrossRef]
34. Huang, P. Material Point Method for Metal and Soil Impact Dynamics Problems. Ph.D. Thesis, Tsinghua University, Beijing, China, 2010.
35. Huang, P.; Zhang, X.; Ma, S.; Huang, X. Contact algorithms for the material point method in impact and penetration simulation. *Int. J. Numer. Methods Eng.* **2011**, *85*, 498–517. [CrossRef]
36. Hu, W.; Chen, Z. A multi-mesh MPM for simulating the meshing process of spur gears. *Comput. Struct.* **2003**, *81*, 1991–2002. [CrossRef]
37. Ma, Z.T.; Zhang, X.; Huang, P. An Object-Oriented MPM Framework for Simulation of Large Deformation and Contact of Numerous Grains. *CMES-Comput. Model. Eng. Sci.* **2010**, *55*, 61–87.
38. Huang, P.; Zhang, X.; Ma, S.; Wang, H.K. Shared memory OpenMP parallelization of explicit MPM and its application to hypervelocity impact. *CMES-Comput. Model. Eng. Sci.* **2008**, *38*, 119–147.
39. Huang, P.; Zhang, X.; Ma, S.; Wang, H. Study on Parallelization of 3D Explicit Matter Point Method Based on OpenMP. *Chin. J. Comput. Mech.* **2010**, *27*, 21–27.
40. Zhang, Y.; Zhang, X.; Liu, Y. An alternated grid updating parallel algorithm for material point method using OpenMP. *CMES-Comput. Model. Eng. Sci.* **2010**, *69*, 143–165.
41. Hornung, R.D.; Kohn, S.R. Managing application complexity in the SAMRAI object-oriented framework. *Concurr. Comput. Pract. Exp.* **2002**, *14*, 347–368. [CrossRef]
42. Ma, J.; Lu, H.; Wang, B.; Roy, S.; Hornung, R.; Wissink, A.; Komanduri, R. Multiscale simulations using generalized interpolation material point (GIMP) method and SAMRAI parallel processing. *Comput. Model. Eng. Sci.* **2005**, *8*, 135–152.
43. Sulsky, D.; Zhou, S.J.; Schreyer, H.L. Application of a particle-in-cell method to solid mechanics. *Comput. Phys. Commun.* **1995**, *87*, 236–252. [CrossRef]
44. Liang, Y.; Zhang, X.; Liu, Y. Extended Material Point Method for the 3D Crack Problems. *Int. J. Numer. Methods Eng.* **2021**, *122*, 3044–3069. [CrossRef]
45. Song, Y.; Liu, Y.; Zhang, X. A non-penetration FEM-MPM contact algorithm for complex fluid-structure interaction problems. *Comput. Fluids* **2020**, *213*, 104749. [CrossRef]
46. Liang, Y.; Zhang, X.; Liu, Y. An Efficient Staggered Grid Material Point Method. *Comput. Methods Appl. Mech. Eng.* **2019**, *352*, 85–109. [CrossRef]
47. Chen, X.; Zhang, X. A Coupled MMALE-FE Method for Solving 3D Fluid-Solid Interaction Problems with Multi-material Flow. *Eng. Comput.* **2019**, *36*, 2766–2786. [CrossRef]
48. Lian, Y.; Zhang, X. A Coupled Finite Element Material Point Method for Large Deformation Problems. In *Advances in Computational Coupling and Contact Mechanics*; Imperial College: London, UK, 2018.
49. Zhang, F.; Zhang, X.; Liu, Y. An augmented incompressible material point method for modeling liquid sloshing problems. *Int. J. Mech. Mater. Des.* **2018**, *14*, 141–155. [CrossRef]
50. Liang, Y.; Benedek, T.; Zhang, X.; Liu, Y. Material point method with enriched shape function for crack problems. *Comput. Methods Appl. Mech. Eng.* **2017**, *322*, 541–562. [CrossRef]
51. Zhang, F.; Zhang, X.; Sze, K.Y.; Lian, Y.; Liu, Y. Incompressible material point method for free surface flow. *J. Comput. Phys.* **2017**, *330*, 92–110. [CrossRef]
52. Liu, P.; Liu, Y.; Zhang, X. Simulation of Hyper-velocity Impact on Double Honeycomb Sandwich Panel and Its Staggered Improvement with Internal-structure Model. *Int. J. Mech. Mater. Des.* **2016**, *12*, 241–254. [CrossRef]

53. Palmer, S.J.P.; Field, J.E.; Huntley, J.M. Deformation, strengths and strains to failure of polymer bonded explosives. *Proc. R. Soc. Lond. A* **1993**, *440*, 399–419.
54. Liu, Q.; Xiao, J.J.; Chen, J.; Ji, G.F.; Zhu, W.; Zhao, F.; Wu, Q.; Xiao, H.M. Molecular Dynamics Simulation on Sensitivity and Mechanical Properties of ε-CL-20 Crystal at Different Temperatures. *Chin. J. Explos. Propellants* **2014**, *37*, 7–17.
55. Zhao, J. Research on microscopic damage and fracture of composite propellant based on global CZM. *J. Solid Rocket Technol.* **2019**, *42*, 269–274.
56. Li, G.; Xing, Y.; Ji, Z.; Xie, L. Finite Element Analysis of Meso-interfacial Debonding of Composite Solid Propellant. *Acta Mater. Compos. Sin.* **2011**, *28*, 229–235.

Disclaimer/Publisher's Note: The statements, opinions and data contained in all publications are solely those of the individual author(s) and contributor(s) and not of MDPI and/or the editor(s). MDPI and/or the editor(s) disclaim responsibility for any injury to people or property resulting from any ideas, methods, instructions or products referred to in the content.